



Rapporti Tecnici INAF INAF Technical Reports

Number	63
Publication Year	2020
Acceptance in OA@INAF	2020-12-11T10:06:16Z
Title	Estimates of system noise temperature in W-band at SRT and effects of beam truncation due to the Gregorian radome
Authors	NAVARRINI, Alessandro; OLMI, LUCA; NESTI, Renzo; BUFFA, Franco; ORLATI, ANDREA
Affiliation of first author	O.A. Cagliari
Handle	http://hdl.handle.net/20.500.12386/28787 ; http://dx.doi.org/10.20371/INAF/TechRep/63

INAF



ISTITUTO NAZIONALE DI ASTROFISICA
NATIONAL INSTITUTE FOR ASTROPHYSICS

Estimates of system noise temperature in W-band at SRT and effects of beam truncation due to the Gregorian radome

¹A. Navarrini, ²L. Olmi, ²R. Nesti, ¹F. Buffa, ³A. Orlati

¹INAF-Osservatorio Astronomico di Cagliari, Selargius (CA)

²INAF-Osservatorio Astrofisico di Arcetri, Firenze (FI)

³INAF-Istituto di Radio Astronomia, Medicina (BO)



Estimates of system noise temperature in W-band at SRT and effects of beam truncation due to the Gregorian radome

Abstract

We report on system noise temperature estimates from the SRT site in W-band (70-116 GHz) based on recorded atmospheric data at four specific days, three-months apart, in the period 15 Oct. 2019-15 July 2020. The estimates are based on the atmospheric model described in [1] and on the feed-horn beams model and receiver noise specification of the W-band multibeam receiver being built for the Gregorian focus of the SRT.

We used different values for the antenna forward efficiency η_f to estimate the impact of such parameter on overall system noise T_{sys} . The beam truncation due to the 1-m diameter SRT Gregorian focus radome, which protects the receiver cabin from the atmospheric agents, is evaluated assuming that the cabin surrounding the radome contributes with a ≈ 293 K thermal noise (greater than the sky noise). The beams from the W-band receiver will be slightly truncated by the radome, especially at the lowest frequencies, where the beams are larger. We conclude that the effects of truncation on T_{sys} are negligible even in the scenario of lowest thermal emission from the sky, expected during winter season.

The estimated seasonal variations of the atmospheric conditions at the SRT show that, for the four specific days for which the system noise temperature was calculated, the T_{sys} have broad minima near the 3 mm band atmospheric window, around ≈ 85 -105 GHz and achieves values of order 100 K or lower during winter. The system noise increases towards the W-band receiver band edges at 70 GHz and 116 GHz; the highest T_{sys} is obtained at the highest frequency of the band, 116 GHz, and reaches values beyond 200 K the 15th of October, 2019 and the 15th of July, 2020.

1. Introduction

The Sardinia Radio Telescope (SRT, www.srt.inaf.it) is a general purpose fully steerable 64-m diameter radio telescope designed to operate with high efficiency across the 0.3-116 GHz frequency range [2]. Since December 2018 the telescope has been opened to the international community to carry out radio astronomy observing programs using an initial set of receivers covering four RF bands across 0.3-26.5 GHz [3]-[7]. The SRT operates in single-dish (continuum, full Stokes and spectroscopy), Very Long Baseline Interferometry (VLBI) and Space Science modes and it has been successfully used also for space-debris detection and Sun observations.

The telescope optical design is based on a quasi-Gregorian configuration with shaped 64-m diameter primary (M1) and shaped 7.9-m diameter secondary (M2) reflectors to minimize spillover and standing waves (see Appendix A for the geometrical details). The primary mirror utilizes an active surface with 1116 electromechanical actuators to compensate the gravitational deformation in real-time. The actuators are also used to convert the shaped surface of the primary mirror to a parabolic profile during primary focus observation.

To extend the current capabilities of the telescope to high frequencies, INAF aims at upgrading the metrology system and at developing and/or procuring a new set of Front-Ends to be installed at its Gregorian focus (Fig. 1). One of such new instruments is the W-band multibeam heterodyne receiver, currently being procured in the framework of the PON-OR1 contract (Programma Operativo Nazionale-Obiettivo Realizzativo n. 1)¹. The W-band multibeam receiver, whose specifications are described in

¹ “Potenziamento del Sardinia Radio Telescope per lo studio dell’Universo alle alte frequenze radio – SRT_HighFreq”, Code PIR01_00010, CUP C87E19000000007.

[8] and in the PON-OR1 Call for Tender documentation, is based on 16 pixels arranged in a square 4×4 configuration; it will be installed at the Gregorian focus of the SRT.

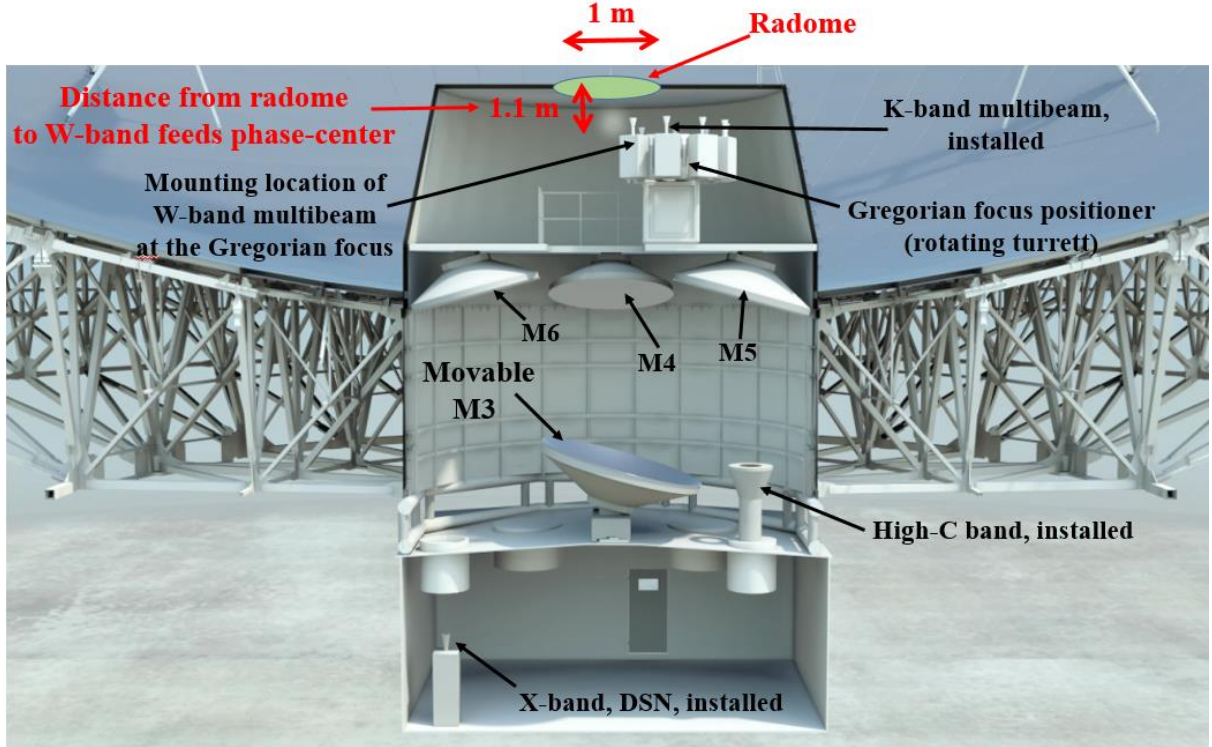


Fig. 1. Cross-cut of the SRT telescope showing details of the three-floor Elevation Equipment Room (EER). The W-band multibeam receiver will be installed on the Gregorian receiver positioner at the Gregorian focus, located on the EER third floor. The beams from the W-band receiver will be slightly truncated by the metallic structure holding the protective 1-m diameter radome, located 1.1 m away from the W-band feed phase-center. The image also shows four of the Beam Waveguide (BWG) mirrors on the EER second floor as well as the BWG foci, one of which on the EER first floor.

The receiver is designed to provide high-efficiency illuminations of the antenna shaped optics for all of its pixels and will deliver a Single Side Band (SSB) receiver noise temperature, referred to the receiver input, of less than $T_{\text{rec}}=75$ K over 80% of the 70-116 GHz band frequency range. The receiver will utilize a heterodyne sideband separating downconversion scheme using W-band mixers with 4-12 GHz IF bands achieving a rejection of the image side band $R_i=G_s/G_i$, $R_i \geq 10$ dB (over 90% of the 4-12 GHz IF band for any RF frequency), where G_s and G_i indicate respectively, the receiver gain in the signal and in the image sidebands. A more typical value of the SSB receiver noise is expected to be $T_{\text{rec}} \approx 60$ K.

The layout of the 4×4 W-band array showing the feed-horn spacing on the focal plane and the beam projection on the sky is shown in Fig. 2. One of the four corner pixels, at the largest distance from the array axis, and one closer to the center are highlighted in red.

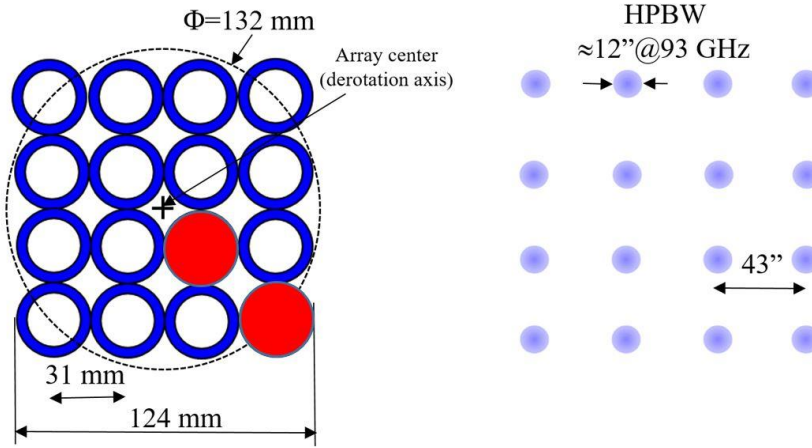


Fig. 2. Configuration of the W-band array with 4×4 feeds on the Gregorian focal plane (left panel) and corresponding beams projected on the sky (right panel). One of the corner pixels and one closer to center are highlighted in red (left panel).

2. Atmospheric modelling at SRT in W-band

The atmospheric modelling for the evaluation of the antenna system noise (T_{sys}) at SRT in W-band was carried out using the program developed by F. Buffa et al., described in [1]. Daily weather forecast model (WRF)² and radiosounding (RDS) data, measured daily at the Decimomannu airport (≈ 30 km from the SRT site), are used by the program to predict the T_{sys} with a molecular absorption model and with the method described by Cortes Medellin in [9]. The program utilizes a numerical weather model to predict both the atmosphere opacity and T_{sys} several hours before a radio astronomical survey. Therefore, it offers the possibility of dynamically scheduling the “best experiment” with respect to the predicted atmosphere status. For the calculation of the system noise temperature (referred to the receiver input) the program adopts the following simplified formula [10] resulting from the recorded atmospheric data:

$$T_{\text{SYS}}(\nu, \varphi) = T_{\text{atm}}(\nu) \eta_f(\nu) [1 - e^{-\tau(\nu) X(\varphi)}] + [1 - \eta_f(\nu)] T_{\text{gnd}} + T_{\text{rec}}(\nu) \quad (1)$$

where the dependence of the various terms from the frequency ν is explicitly indicated:

- $\eta_f(\nu)$: forward efficiency, defined later. This is the feed forward efficiency, i.e. the fraction of received power coupled to the sky, in contrast to the fraction of power coupled inside the receiver cabin or to ground (for primary focus receiver);
- $\tau(\nu)$: zenithal sky opacity;
- $T_{\text{atm}}(\nu)$: effective temperature in atmosphere or mean radiative temperature of atmosphere;
- $X(\varphi)$: air mass at φ zenith angle or co-elevation (a simple and commonly adopted air mass approximation is $X(\varphi) = \sec \varphi = 1/\cos(\varphi)$). The co-elevation angle φ is the antenna pointing direction and is defined as $\varphi = 90^\circ - \theta$, where θ is the elevation angle;
- T_{gnd} : ground level temperature (for primary focus receiver), or Gregorian cabin internal temperature (for secondary or BWG focus receiver), assumed to be 293 K;
- $T_{\text{rec}}(\nu)$: Single Side Band receiver noise temperature. For our estimates, we use the simplified assumption that the T_{rec} of the W-band multibeam receiver under development for the SRT is frequency-independent and of order 60 K.

² In collaboration with the Sardinia Department for the hydro-weather forecast (ARPAS).

The use of the forward efficiency and T_{gnd} in eq. (1) is based on various simplifying assumptions which are more appropriate when analysing prime-focus configurations. In the next sections we address the validity of these assumptions and propose some modifications in eq. (1).

2.1 Antenna beam pattern

A typical radiation pattern of the SRT antenna illuminated from the secondary focus, computed over a very wide angular range, is shown in Fig. 3. The beam pattern was obtained through a GRASP simulation by considering the contributions of the electromagnetic fields from the feed and from the two mirrors (secondary and primary) that scatter the radiation throughout the entire solid angle.

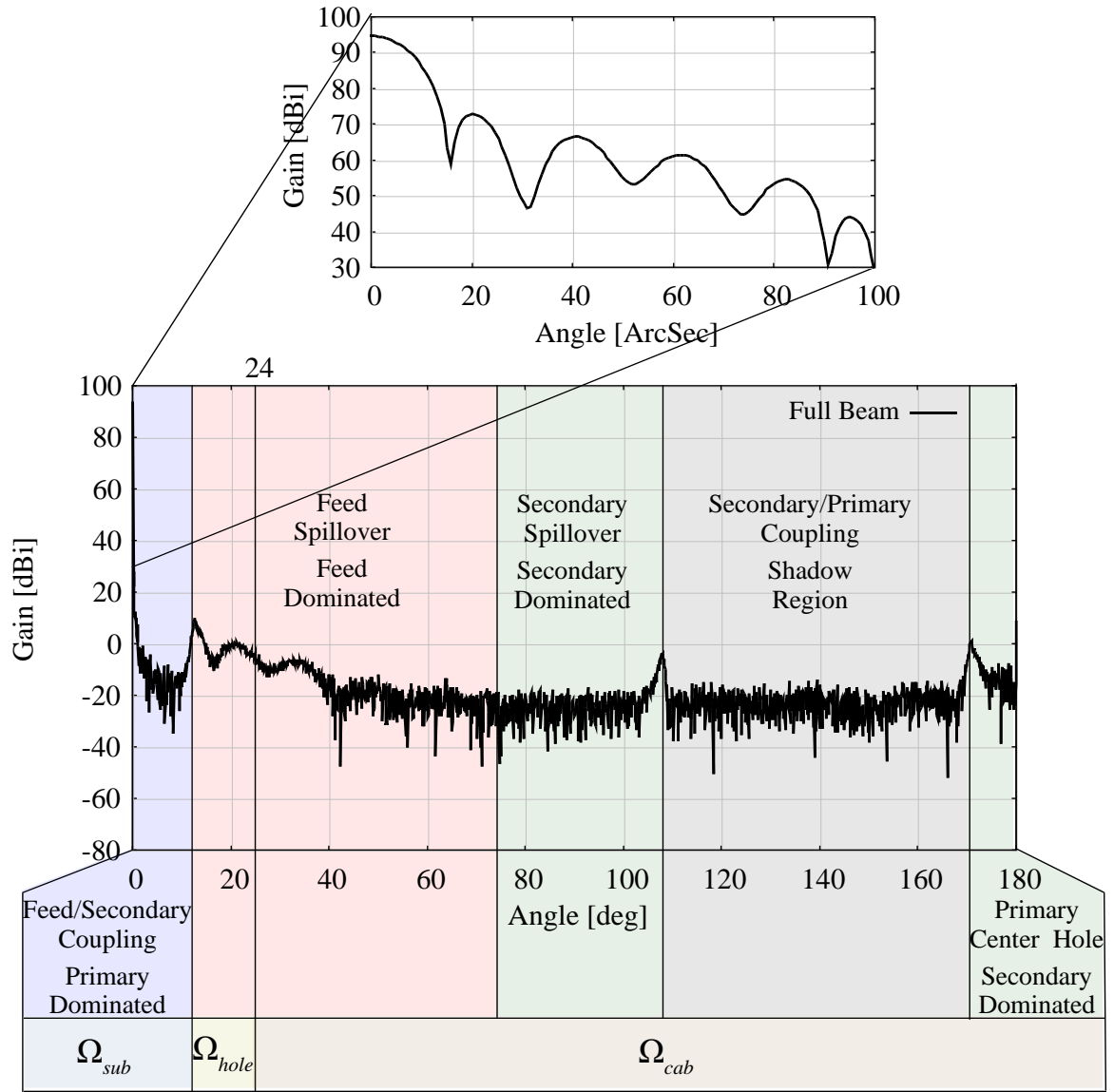


Fig. 3. Far-field radiation pattern at 93 GHz (only one cut shown) of the Sardinia Radio Telescope illuminated with a W-band feed-horn from the Gregorian focus. The antenna gain was calculated with GRASP across the full 180 deg angle (lower graph). The inset in the upper graph shows the simulation result in the very narrow angular region within 100 arcsec from boresight, and contains the relevant part of the diffraction pattern around the main lobe. The lower graph illustrates the contribution to the total antenna gain at different angular regions to the boresight. The angle at which the antenna beam intercepts the edge of the receiver cabin is 24 deg.

Heavy computational time was required for the accurate electromagnetic analysis of the full 180 deg angle antenna-beam-cut of the Gregorian configuration of SRT at 93 GHz frequency³.

The analysis across the whole 180 deg angle allowed us to highlight the contributions of the different scatterers (the feed and the two mirrors) in the various angular ranges. The results of such an analysis is representative of all the receivers installed in the Gregorian focus, independently from their operative frequency, as the feeds of the different receivers are optimized to provide similar illumination patterns and edge tapers in different bands. The main difference in the beam patterns resulting from different Gregorian focus receivers is only in the very narrow region around the optical axis, where at different frequencies, the gain curve is different in both shape and level (the boresight gain of an ideal antenna scales up with the square of the frequency). The main lobe and the few secondary lobes around the small 100 arcsec region from boresight are shown in the zoomed plot on the top part of Fig 3. The frequency-dependent antenna gain and the full-width at half maximum (FWHM) at 93 GHz are, respectively of order 94.5 dBi and 12 arcsec.

Fig. 3 shows that the SRT illumination pattern can be divided into five main regions, corresponding to various off-boresight angles, where the boresight is the direction of antenna maximum gain at $angle=0\ deg$ (see Appendix A for the geometrical details of the SRT antenna):

- $0\ deg \leq angle \leq 12\ deg$: the region around the optical axis, extending up to the subreflector half angle (the subreflector edge is seen from the Gregorian focus at 12 deg half angle). In this angular region the illumination pattern is dominated by the contribution of the radiation scattered by the primary mirror. This region is indicated as “Feed/Secondary Coupling, Primary Dominated” and includes the diffraction pattern Ω_d (described in Appendix E) corresponding to a narrow angular region around the main lobe. The diffraction pattern region is within $\Omega_{sub} + \Omega_{hole}$, as shown in Fig. 3;
- $12\ deg \leq angle \leq 75\ deg$: the region between the subreflector edge angle (12 deg) and the angle $\alpha_{FS} \approx 75\ deg$ at which the irradiation from the secondary mirror dominates over the feed radiation⁴. In this angular region the feed radiation pattern, which is not coupled through the optics, dominates the radiation pattern of the entire antenna. This region is indicated as “Feed Spillover, Feed Dominated”;
- $75\ deg \leq angle \leq 106\ deg$: a region between $\alpha_{FS} \approx 75\ deg$ and the edge of the primary mirror at $\approx 106\ deg$ indicated as “Secondary Spillover, Secondary Dominated”. We note that $106\ deg = 180\ deg - 74\ deg$ is the half angle corresponding to the primary mirror edge seen by the secondary mirror position, in the Gregorian focus reference system;
- $106\ deg \leq angle \leq 176\ deg$: a region beyond $\approx 106\ deg$, extending up to $\alpha_{CH} \approx 176\ deg$, indicated as “Secondary/Primary Coupling, Shadow Region”. The angle α_{CH} corresponds to the half angle subtended by the edge of the “Central Hole” (CH) of the primary mirror (as seen by the secondary mirror position, in the Gregorian focus reference system). In the GRASP model, the central hole is assumed to be 7.9 m in diameter;
- $176\ deg \leq angle \leq 180\ deg$: an angular region beyond $\alpha_{CH} \approx 176\ deg$, extending up to the $\approx 180\ deg$, indicated as “Primary Center Hole, Secondary Dominated”.

³ A complete GRASP simulation at 93 GHz of a single beam cut across the full 180 deg angular region requires about 15 days on a powerful desktop computer.

⁴ The plot on the lower graph of Fig. 3 shows a relatively flat antenna power pattern with no obvious transition between different “regions” at $\approx 75\ deg$ angle, where the total antenna gain is of order -25 dBi. The electromagnetic simulations conducted with GRASP have allowed to decompose the independent contributions to the total irradiation resulting from the feed, from the secondary and from the primary mirror. The GRASP simulations showed that in the angular range between $\approx 12\ deg$ and $\approx 106\ deg$, the main contributions to the total antenna beam pattern is due to the feed (for angles $12\ deg \leq angle \leq 75\ deg$) and to the secondary mirror (for angles $75\ deg \leq angle \leq 106\ deg$). It is beyond the scope of this memo to discuss the independent contributions to the total power pattern of the antenna.

The upper plot of Fig. 3 shows the shape of the main beam and of the first few sidelobes. The first sidelobe (at ≈ 72 dBi) is approximately 23 dB below the main beam lobe (boresight gain ≈ 94.5 dBi). Beyond the 12 deg angle, in the “Feed Spillover, Feed Dominated” region, the radiation pattern has a maximum of ≈ 7 dBi (peak of feed spillover at ≈ 13 deg angle). This is ≈ 87 dB below the boresight gain! The antenna gain in the angular range $\approx 20 \text{ deg} \leq \text{angle} \leq 180 \text{ deg}$ is less than 0 dBi (this includes the region with backward coupled radiation at $90 \text{ deg} \leq \text{angle} \leq 180 \text{ deg}$).

Therefore, the total antenna beam pattern includes the scattering of the radiation from the subreflector that is not intercepted by the primary mirror. This fraction of power is directed towards the ground and can be associated to the spillover of the field scattered by the secondary mirror outside the edge of the primary mirror. This fraction of power is not taken into account in our estimates of the system noise temperature, which are derived according to eq. (1), as discussed below.

From the point of view of the interaction of the antenna beam with the environment, with the aim of estimating T_{sys} , three different angular regions have been considered. These regions are highlighted at the bottom of Fig. 3:

- Ω_{sub} : $0 \text{ deg} \leq \text{angle} \leq 12 \text{ deg}$: where the antenna beam dominated by the irradiation of the primary mirror is coupled to the sky;
- Ω_{hole} : $12 \text{ deg} \leq \text{angle} \leq 24 \text{ deg}$: where the antenna beam dominated by the irradiation of the feed is coupled to the sky through the hole of the cabin;
- Ω_{cab} : $24 \text{ deg} \leq \text{angle} \leq 180 \text{ deg}$: where the antenna beam is dominated by the irradiation of the feed or the subreflector. The feed part is coupled to the cabin, while the subreflector part is coupled mainly to the ground. In the evaluation of T_{sys} we will consider only the feed coupling to the cabin, which is predominant.

2.2 Further considerations on T_{sys}

The simplified formula for the calculation of T_{sys} , eq.(1), can be derived from the exact definition of antenna temperature when the antenna is pointed at the blank sky. An early example of derivation of eq. (1) is discussed by Kutner & Ulich [11] (KU, hereafter). The formula derived by KU was based on the definition of forward efficiency η_f . However, in cases where spillover and scattering may have different origins, as discussed in the previous section, a different definition of efficiency to be used in eq. (1) may be required. We therefore re-write eq. (1) in a slightly more general form (see Appendix E), where η_f is replaced by η_{feed} and T_{gnd} is replaced by T_{spill} :

$$T_{\text{SYS}}(\nu, \varphi) = T_{\text{atm}}(\nu) \eta_{\text{feed}}(\nu) [1 - e^{-\tau(\nu)X(\varphi)}] + [1 - \eta_{\text{feed}}(\nu)] T_{\text{spill}}(\nu) + T_{\text{rec}}(\nu) \quad (2)$$

The feed efficiency $\eta_{\text{feed}}(\nu)$ is the ratio of the feed radiation coupled to the sky (also by means of the optics) over the feed radiation integrated over the entire 4π solid angle. Appendix E shows that, in our approximation, $T_{\text{gnd}} \approx T_{\text{spill}}$.

We note that a skydip procedure allows to directly measure the efficiency factor η_{feed} in eq. (2), independently from the exact model adopted for the spillover termination. However, the temperature T_{spill} assumed in eq. (2) is associated to the feed spillover. In the simplified model described in Appendix E, the cabin contribution to the thermal noise is independent of the antenna pointing direction and this is the case also for the portion of the feed efficiency η_{feed} associated to it. However, in the real antenna system this is not strictly true. Since the beam radiated by the feed and coupled through the antenna optics is ideally always the same in the antenna reference system, it is expected that the feed forward efficiency will depend on the antenna pointing direction, as the fraction of the beam coupling to the sky is pointing direction-dependent. This kind of effect can be considered negligible in the SRT case, since almost all of the energy captured by the antenna comes from a very small angle concentrated around the antenna pointing direction.

Furthermore, in a real system, the feed forward efficiency dependence on the elevation angle is also due to: *a)* the change in the relative positions among the feed, the primary and secondary mirrors during antenna movements, for example during source tracking; and *b)* the deformation of the mirrors, all caused by gravitation, thermal effects and wind. Also, these effects can be considered negligible for SRT. In this regard, the gravitational effects of the SRT primary mirrors are compensated by the active surface.

Assuming all of these minor effects can be considered negligible, we will continue to use eq. (2) using the standard forward efficiency, although η_f should be replaced with the effective feed efficiency, η_{feed} , if known.

Eqs. (1) and (2) assume there is no contribution to the system noise from the image side band, i.e. it applies to a receiver with an ideal sideband rejection $R_i \rightarrow \infty$. In case the sideband rejection is finite, the single side band system noise temperature on the right side of eq. (1) must be multiplied by a factor $(1+1/R_i)$, with R_i expressed in linear value, rather than in dB (the dependence from the frequency ν is not explicitly indicated for equation's compactness):

$$T_{SYS}(\varphi) = (1 + 1/R_i) \{ T_{atm} \eta_f [1 - e^{-\tau X(\varphi)}] + (1 - \eta_f) T_{gnd} + T_{rec} \} \quad (3)$$

The relatively high sideband rejection specified for the W-band multibeam receiver, $R_i \geq 10$ dB (equivalent to ≥ 10 in linear scale), allows to strongly reduce the atmospheric noise contribution in the image sideband during spectral line observations. In an atmospheric environment in which the system noise is dominated by the atmosphere, rather than by the receiver noise, a mixer with ideal “infinite” rejection allows to halve the system noise, if compared by a Double Side Band (DSB) mixer that delivers no rejection, $R_i = 1$.

Therefore, the adopted formula with “ideal rejection” for the system noise will predict the value to within 10% of the expected SSB value, i.e. the T_{sys} will be within 1.1 (worst case) of the value provided by eq. (1). The value of R_i predicted for the W-band multibeam receiver is frequency dependent and expected to fall in the range 10-20 dB. We note that the effects of the finite image sideband rejection on the system noise, in case $R_i \approx 10$ -20 dB, will have an impact of order 1% to 10% on T_{sys} . These values are of the same order of magnitude (or greater) of the beam truncation effects discussed further down.

One of the main goals in the optimization of the performance of a receiving system is to decrease the system noise and to maximize the antenna effective area A_{eff} , as the measure of the telescope performance is the ratio A_{eff}/T_{sys} . For given atmospheric conditions and fixed receiver noise temperature T_{rec} , the greater R_i , the lower T_{sys} . When possible, beam truncation effects should also be reduced. Typically, the clearance diameter of all optical elements of the receiver cryostat (Infrared filter, vacuum window, quasi-optical elements – if used, etc.) and of the apertures in front of the receiver RF optical path (like the radome at the antenna vertex) should be at least 4 beam radii at the lowest observing frequency (where the beam is larger) to incur in negligible truncation loss (the beam radius is the 1/e amplitude of the best fit Gaussian beam). When the beam is truncated there are two types of loss: the power that is stopped by the aperture and the power that is scattered (diffracted). For small losses, these two are approximately equal [12]. Hence, if a beam is vignetted such that –20 dB of the power is intercepted by the stop, then the loss will be ~2 %, half on each side of the aperture. The added noise should be calculated taking into account where the stopped (absorbed or reflected) and diffracted power will be terminated.

We note that while the beam truncation depends on the feed-horn radiation pattern and on the size and relative positions of the truncating elements along the RF signal path (infrared filter, cryostat vacuum window, Gregorian radome, optical elements, etc.), the image sideband rejection depends on: *a)* the receiver architecture (mechanically tuned single sideband mixer, image rejection mixer with waveguide or quasi-optical filter, sideband separating mixer, etc.); *b)* the specific mixer rejection performance; and

on c) the receiver passband flatness. While the beam truncation and image sideband are unrelated, their effects modify the single side band system noise temperature through eq. (3).

Another assumption we made in eqs. (1)-(3) is that the contribution to the system noise from the Cosmic Background Radiation (CMB) of 2.73 K can be neglected.

The graphical interface of the program described in [1], allowing to calculate T_{sys} based on eq. (1), is illustrated in Fig. 4. The input parameters are the “Epoch” (set to 15 January 2020 in the example), the frequency in GHz “Freq”, the antenna elevation pointing angle “Theta” (where $\theta=90$ deg corresponds to the Zenith), the value of the feed forward efficiency η_f , “eta”, and the receiver noise temperature “Trec” (60 K in the example). As mentioned earlier, in the most general case the forward efficiency should be replaced with the effective feed efficiency, η_{feed} , if known.

3. System noise dependence from forward efficiency and beam blockage

The system noise was calculated for different values of forward efficiency in order to evaluate the effects of the blockage due to the metallic structure surrounding the 1-m diameter radome, located at a distance of 1.1 m from the feed-horn array phase-center on the Gregorian focal plane (see Figs. 1 and 5). The currently used version of the radome, visible on the right panel of Fig. 5, consists of 8 cm thick cylindrical structure, 1-m in diameter, made of Styrodur 3035CS. This extruded expanded polystyrene is covered with a water-repellent protective layer. The radome assembly, described in [13], is transparent to the microwave and millimetre-wave radiation and determines negligible signal loss. The diameter of the radome was chosen as a trade-off between the widest possible value that would allow negligible truncation of the beams and the need of maintaining the required mechanical properties (like stiffness) and ease of maintenance of the radome assembly, while also guaranteeing low loss (the insertion loss increases with material thickness).

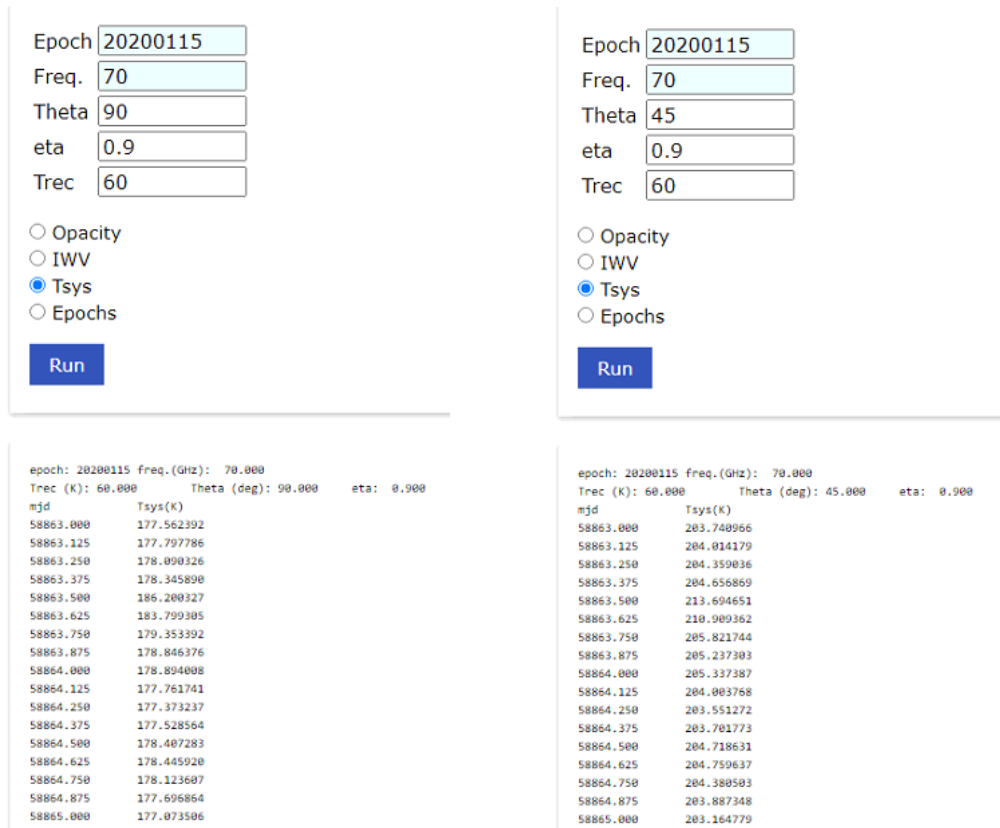


Fig. 4. System noise estimates at 90 deg (left) and 45 deg elevations (right) at 70 GHz as a function of time expressed in Julian Days. Atmospheric data of January 15, 2020.

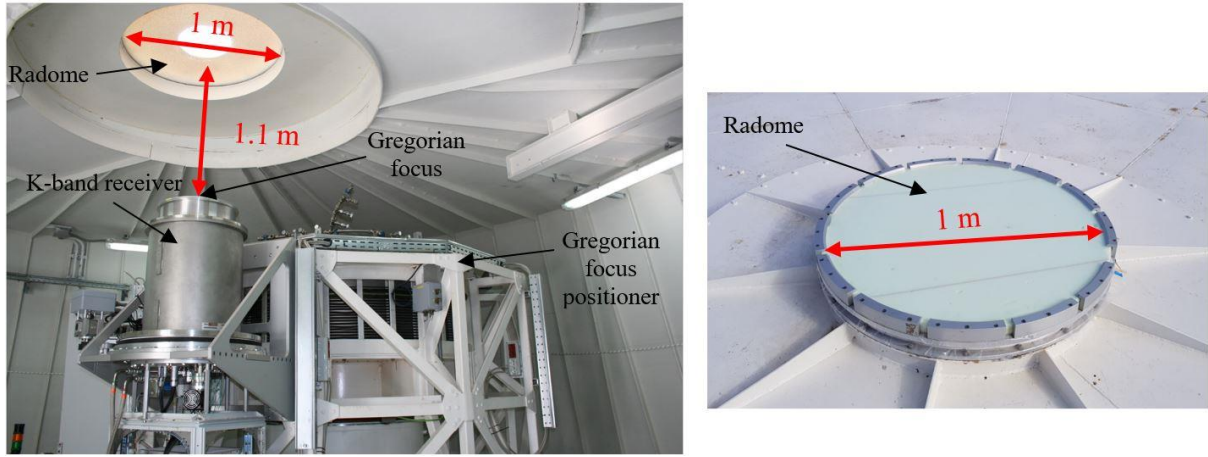


Fig. 5. Photo of the Gregorian receiver cabin showing the K-band receiver with feed array phase-center located 1.1 m below the 1-m diameter radome (left). During observations in W-band, the multibeam receiver will be positioned in focus by the “Gregorian focus positioner”, at the location occupied by the K-band receiver. Photo of the radome taken from above the receiver cabin (right).

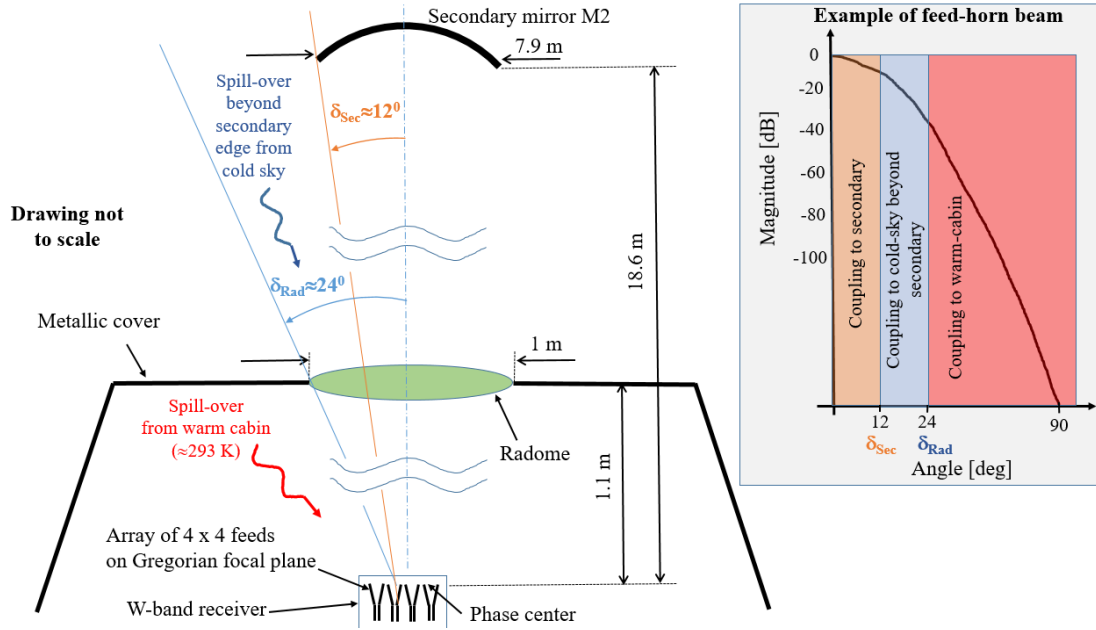


Fig. 6. Left: Schematic of the Gregorian receiver cabin showing W-band receiver feed-horns phase-center at 1.1 m from the radome and 18.6 m from the secondary mirror edge. Each feed sees the edge of the radome and of the secondary mirror to an angle of, respectively $\delta_{\text{Rad}} \approx 24$ deg and $\delta_{\text{Sec}} \approx 12$ deg from the optical axis. Right: example of feed-horn beam illumination showing the coupling to the secondary mirror, to the cold sky beyond the secondary and to the warm receiver cabin (at ≈ 293 K). The illumination function includes neither the feed-horn sidelobes nor any of the frequency-dependent beam-pattern features of a real feed-horn, but serves only as simplified illustration.

Fig. 6 illustrates a schematic of the receiver cabin and an example of the feed-horns response versus angular directions δ . The edges of the secondary mirror and of the radome are seen under angles of, respectively $\delta_{\text{Sec}} \approx 12$ deg and $\delta_{\text{Rad}} \approx 24$ deg. For angular directions $\delta < \delta_{\text{Sec}}$ the feed-horn beam couples efficiently to the antenna secondary mirror M2, through the radome, and is then coupled to the cold sky. A small fraction of the beam power passing through the radome is spilled out of the secondary and it is also coupled to the cold sky, in a region comprised between angular directions $\delta_{\text{Sec}} \approx 12$ deg and

$\delta_{\text{Rad}} \approx 24$ deg, while another small fraction of the beam power is coupled to the ≈ 293 K warm receiver cabin for angles greater than $\delta_{\text{Rad}} \approx 24$ deg. The contribution from beam directions $\delta_{\text{Sec}} < \delta < \delta_{\text{Rad}}$ is approximated to be coupled to the same temperature of cold sky as the one from the antenna pointing direction ($\delta < \delta_{\text{Sec}}$) so that both contributions can be simply characterized by the efficiency parameter η_f . Under this approximation, the first contribution on the right side of eq. (1) is slightly under-estimated for all the antenna pointing directions and allows to obtain a worst-case estimate of the cabin contribution as a percentage of the overall system temperature.

The minimum pointing elevation angle at SRT is $\theta_{\text{min}} = 6$ deg. When the antenna pointing direction is close to the horizon, i.e. $\theta_{\text{min}} < \theta < \theta_{\text{min}} + \delta_{\text{Rad}}$ (6 deg $< \theta < 30$ deg) the power coupled into the feed-horns from beam directions $\delta_{\text{Sec}} < \delta < \delta_{\text{Rad}}$ will include contributions not only from the cold sky, but also from the “warm” ground. In this case, the coupled power into the receiver will also depend on the Azimuthal angle “ Az ”, because of the specific topographic reliefs around the SRT area, which includes hills of different height and flatter terrains that are seen under different angles from the SRT feed-horns phase centres. A precise estimate of the system noise at these low elevation angles would require to account of the orography at the SRT site and would provide T_{sys} values that depend, in addition to frequency, on the co-elevation and on Azimuth angle, $T_{\text{sys}}(\varphi, Az)$. Providing an estimate of T_{sys} at low elevation angles is beyond the scope of this technical report. To obtain the estimates given in this manuscript, we assume that the antenna pointing direction will be at elevation angles away from the horizon, i.e. with $\theta > \theta_{\text{min}} + \delta_{\text{Rad}} = 30$ deg, equivalent to pointing directions 30 deg $< \theta < 90$ deg. This is expected to be a commonly chosen situation when selecting the radio astronomy targets to observe, as the system noise temperature is strongly elevation dependent (see eq. (1)) and the observation sensitivity is minimized when the source is closer to the Zenith.

The second contribution on the right side of eq. (1), associated to the fraction of the beam power that illuminates the metallic structure of the cabin beyond the radome edge, which is mainly contained in the beam sidelobes of the feed, constitutes the term we are mainly interested to evaluate in this work.

The fraction of the radiation from the illuminating feeds reflecting off the cabin metallic structure is scattered inside the antenna elevation equipment room. In the system noise calculations discussed further down, it is assumed that such scattered radiation is terminated to the ≈ 293 K physical temperature of the cabin. Therefore, the beam truncation adds extra noise to the system (because a fraction of the radiated beam sees a ≈ 293 K black-body rather than the cold sky) and leads to diffraction in the antenna beam pattern. The truncation of the beam at the angle of the radome edge δ_{Rad} for the feed designed by UKRI (United Kingdom Research and Innovation), which was awarded the contract of fabrication of the W-band receiver, is at the level of ≈ -20 dB at 70 GHz. The level of truncation decreases quickly with increasing frequencies (≈ -33 dB at 93 GHz and ≈ -45 dB at 116 GHz). The radiation from the feeds bouncing back from the metallic structure surrounding the radome (and from the radome itself, if not properly designed) might determine a standing-wave pattern on the signal band whose maxima are separated by ≈ 140 MHz, as a result of the two not perfectly matched items (the feed-horn on one end and the radome metallic structure on the other end). The periodicity of the standing wave pattern $\nu_{\text{sw}} \approx 140$ MHz corresponds to twice the electrical length between the two mismatched items, $\lambda_{\text{sw}} \approx 1100$ mm (see Figs. 5 and 6), i.e. $\nu_{\text{sw}} = c/(2 \lambda_{\text{sw}})$, where c is the speed of light in air. The diffraction effects and the standing-wave pattern can be reduced by covering the inner parts of the cabin around the radome aperture with radiation-absorbent material (for example Eccosorb). The effects of blockage, diffraction and standing waves are expected to be larger at the lowest frequency of the W-band, around 70 GHz, where the beam is larger.

3.1 System noise estimates assuming $\eta_f=0.9$ and $\eta_f=1$

The system noise was calculated assuming $T_{\text{rec}}=60$ K, for 90 deg and 45 deg elevations, using the atmospheric data estimated on Jan. 15th, 2020, and supposing a frequency-independent forward efficiency with value $\eta_f=0.9$. The value of the receiver noise T_{rec} is the contractual one established with UKRI for weak radio astronomy source observation mode: The W-band receiver pixel elements shall provide a single sideband noise performance, inclusive of sideband rejection, of $T_{\text{rec}} < 60$ K per sideband across 80% of the RF bandwidth extending from 75 GHz to 116 GHz. The receiver shall also exhibit a single sideband noise performance of $T_{\text{rec}} < 100$ K across the full RF bandwidth of 70 GHz to 116 GHz, i.e. at any frequency point within this band. The value of $\eta_f=0.9$ is a “worst case” scenario, as we will discuss in next subsection.

The results of the T_{sys} estimates at 70 GHz show that the average value is approximately 178 K@90 deg elevation and 205 K@45 deg elevation, as illustrated in the tables of Fig. 4.

Estimates of T_{sys} at 75 GHz, 93 GHz and 116 GHz frequencies (under the same assumption $\eta_f=0.9$ e $T_{\text{rec}}=60$ K) at the two elevations of 90 deg and 45 deg are presented respectively in Figs. B1, B2 and B3 of Appendix B.

Similar T_{sys} estimates were carried out under the assumption of unitary forward efficiency $\eta_f=1$, i.e. when all power is coupled to the cold sky (and no power is coupled to the Gregorian receiver cabin). The results will be presented further down.

3.2 System noise estimates using η_f calculated from GRASP

The $T_{\text{sys}}(\nu, \varphi)$ was calculated at 90 deg and 45 deg elevations for the atmospheric data recorded on Jan. 15th, 2020, this time using the realistic value of the frequency-dependent feed forward efficiency $\eta_f(\nu)$ calculated by UKRI. The value of $T_{\text{rec}}=60$ K was adopted. The forward efficiency was calculated using the GRASP electromagnetic software, which allows performing accurate optical analysis of the coupling between the illuminating feed-horn and the SRT optics. The feed-horn was optimized to provide optimum illumination parameters of the SRT. The results of the UKRI simulations are presented in [14]. The values of the frequency-dependent Relative Truncated Power (RTP) of the W-band receiver beams due to the finite aperture of the radome (1-m diameter) are listed in Table 1. RTP is the integral of the power coupled inside the cabin that does not exit the 1-m diameter vertex hole, i.e. the power radiated at angles $\delta > \delta_{\text{RAD}}=24$ deg.

They were calculated for the corner pixels illustrated in Fig. 2 and only at four frequencies 70, 75, 93 and 116 GHz, due to high computation time.

Frequency [GHz]	RTP for corner pixel
70	0.042
75	0.03
93	0.011
116	0.005

Table 1. Relative Truncated Power (RTP) calculated using GRASP by UKRI for the FH2 corner feed-horn of the W-band array. The beam is slightly truncated by the 1-m diameter radome. The truncation is larger (4.2%) at the lowest frequency of the band (70 GHz). The calculation refers to the 1-m diameter radome located at 1.1 m from the feeds phase-centers.

The values of truncation are greater at the lowest frequency (70 GHz), where the beam is larger. There is a very minor difference when considering a corner pixel and a pixel closer to the center (both illustrated in Fig. 2). For example, at 70 GHz, RTP=0.042 for the corner pixel and RTP=0.041 for the

closer-to-center pixel. All the remaining calculations are performed for the worst-case situation of the corner pixel.

The RTP value is related to the feed forward efficiency through the simple simplified formula:

$$\eta_f(\nu) = 1 - \text{RTP}(\nu) \quad (4)$$

where it is assumed that the power that comes out of the 1-m diameter hole at the vertex is radiated towards the sky, while the spill-over from the primary mirror, i.e. the power reflected towards the ground by the secondary mirror (rearward spill-over) is neglected. If the rearward spill-over were taken into account, the forward efficiency would be slightly smaller than calculated.

Starting from the four η_f values at 70, 75, 93 and 116 GHz derived with GRASP (see Table 1), we performed a fit to the data and obtained the forward efficiency at all frequencies across 70-116 GHz. We used a non-linear symmetrical sigmoidal fit, whose plot and equation are given in Fig. 7.

The system noise estimates at 70, 75, 93 and 116 GHz, for elevation angles 90 deg and 45 deg, are given respectively, in Fig. 8 and Fig. 9. The plots show the dependency from the forward efficiency values, where the system noise decreases with increasing forward efficiency.

The summary of the results is shown in Fig. 10, where all plots are over imposed on the same graph. These plots were generated from the numerical values of Tab. 2, which also gives the fractional variation of the system noise due to the radome in the last two table columns. Here, the relative variation is derived with respect to the situation of $\eta_f=1$. The plots of Fig. 10 and the results of Tab. 2 show that the effects of the beam truncation on T_{sys} due to the radome are $\approx 4\%$ and $\approx 3\%$ respectively at 90 deg and 45 deg elevations at 70 GHz, where the beam truncation is greater. At 75 GHz, the corresponding fractional variation are $\approx 6\%$ and $\approx 3\%$. We note that, even if the beam truncation is larger at lower frequencies, the relative increase of T_{sys} at 90 deg elevation is greater at 75 GHz ($\approx 6\%$) than at 70 GHz ($\approx 4\%$) because the atmosphere is cooler (at 75 GHz). The relative variations of T_{sys} at 90 deg elevation due to beam truncation at 93 GHz and 116 GHz are respectively, 2.6% and 0.5%. For all frequencies, the relative variation decrease when the airmass increases (from 90 deg to 45 deg elevation) as indicated in Table 2.

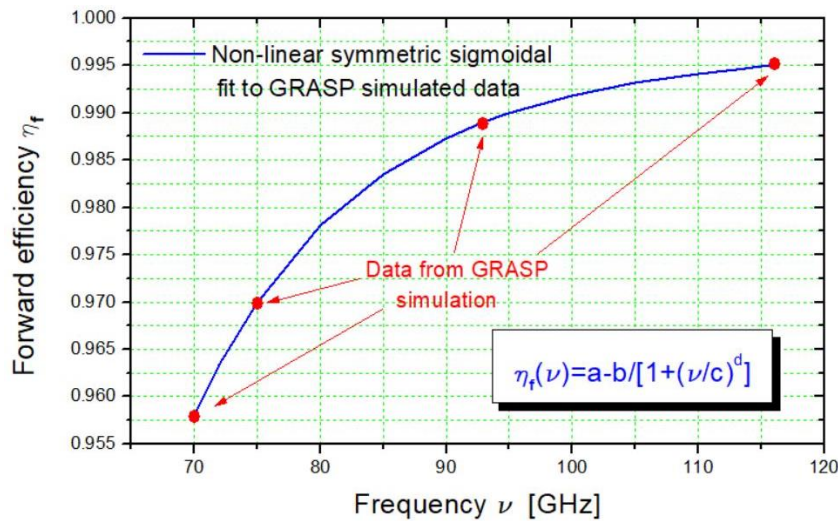


Fig. 7. Non-linear symmetrical sigmoidal fit to the four forward efficiency data values calculated by UKRI with the GRASP electromagnetic software. The coefficient in the formula given in the inset are the following: $a=0.997$, $b=0.426$, $c=46.92$, $d=5.7$.

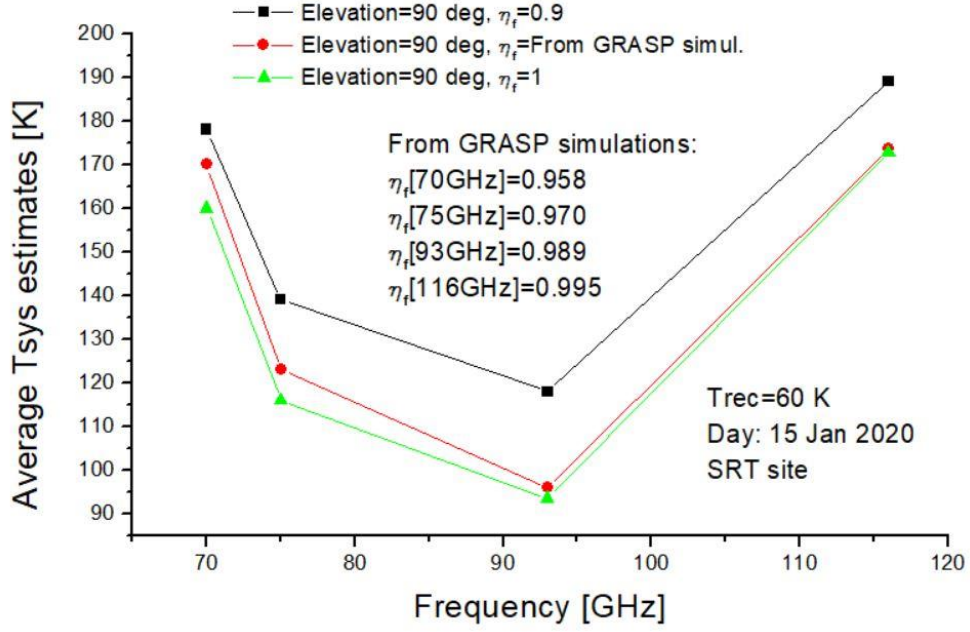


Fig. 8. System noise versus frequency calculated at 90 deg elevation for the atmospheric data recorded on Jan 15, 2020 at the SRT site, assuming $T_{\text{rec}}=60$ K, using forward efficiency values η_f of 0.9, 1 and calculated by GRASP.

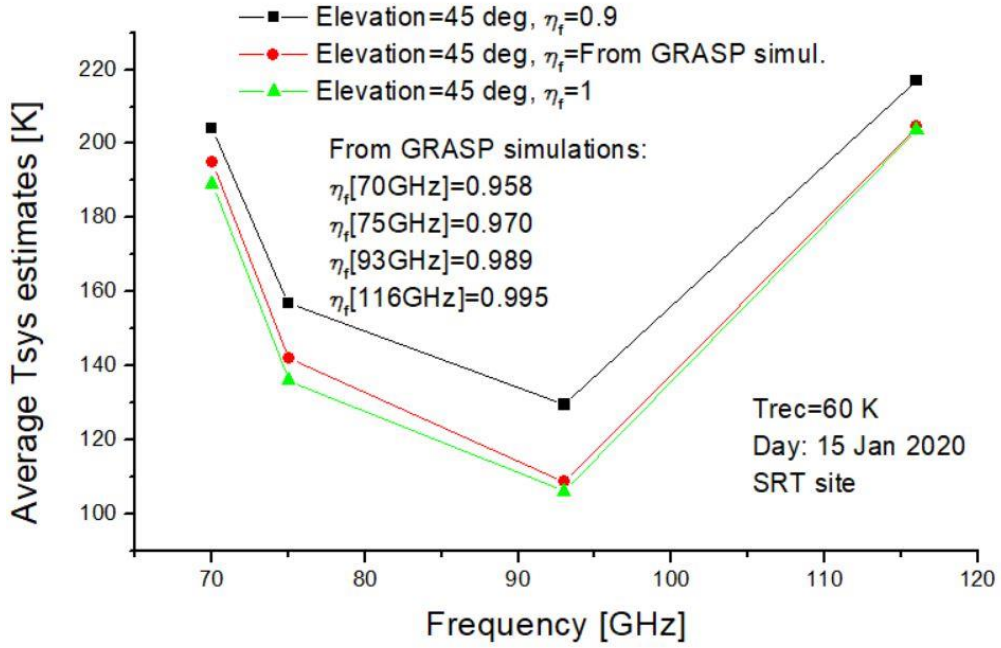


Fig. 9. System noise versus frequency calculated at 45deg elevation for the atmospheric data recorded on Jan 15, 2020 at the SRT site, assuming $T_{\text{rec}}=60$ K, using forward efficiency values η_f of 0.9, 1 and calculated by GRASP.

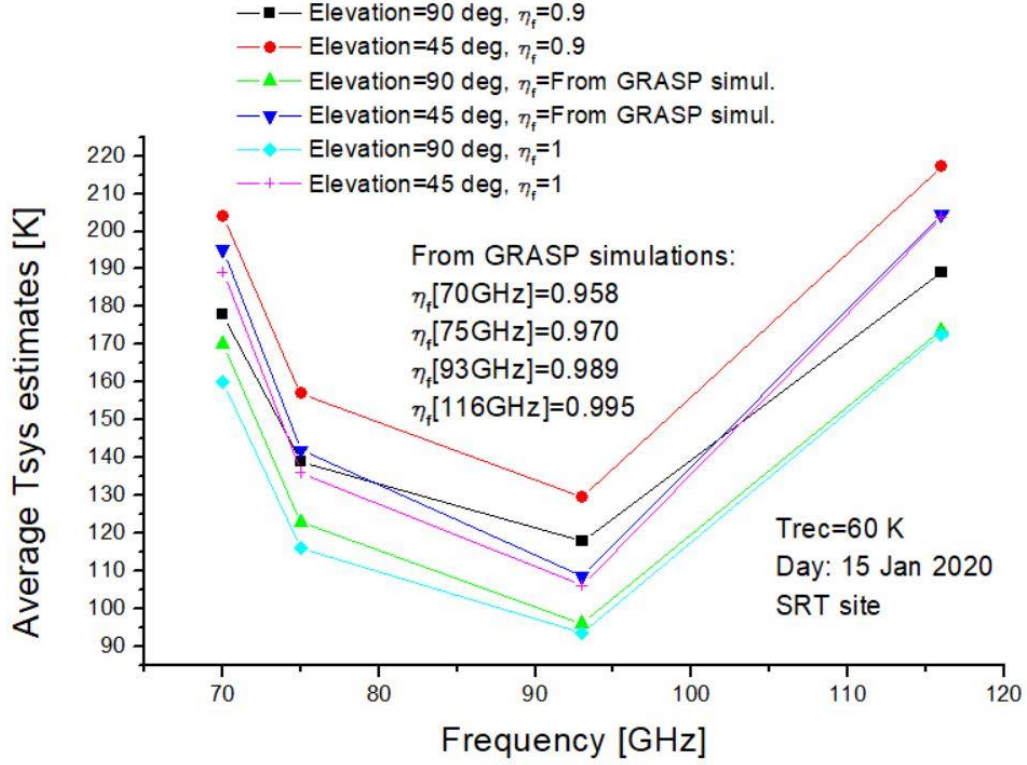


Fig. 10. System noise versus frequency calculated at 90 deg and 45 deg elevations for the atmospheric data recorded on Jan 15, 2020 at the SRT site, assuming $T_{rec}=60$ K, using forward efficiency values η_f of 0.9, 1 and calculated by GRASP.

Frequency [GHz]	System noise T_{sys} [K]						$\Delta T_{sys}/T_{sys}$ El=90 deg [%]	$\Delta T_{sys}/T_{sys}$ El=45 deg [%]
	El=90 deg $\eta_f=0.9$	El=45 deg $\eta_f=0.9$	El=90 deg η_f From GRASP	El=45 deg η_f From Grasp	El=90deg $\eta_f=1$	El=45 deg $\eta_f=1$		
70	178	204	167.7	195.6	160	189	4	3
75	139	157	123	142	116	136	6	3
93	118	129.5	96	108.7	93.5	106.2	2.6	2.3
116	189	217	173.6	204.5	172.7	203.7	0.5	0.3

Tab. 2. Numerical values of system noise temperature versus frequency at 90 deg and 45 deg elevations calculated for the different forward efficiency η_f values discussed in the text. The last two columns provide the relative variation of T_{sys} when the system noise is calculated using η_f from GRASP simulations and using the “ideal” $\eta_f=1$.

4. Estimate of seasonal dependency of system noise temperature

A radio astronomy atmospheric site quality depends on many parameters, including altitude, local weather pattern, wind, water vapour content, etc. The atmospheric opacity and system noise temperature across W-band are time and frequency dependent due to the Integrated Water Vapour (IWV) and Integrated Liquid Water (ILW) variations on short time-scale (daily variation) and seasonal time-scale (seasonal variation). The weather statistics at the SRT site are described in Nasir et al. [15]. Although it is not possible to predict with precision these quantities on long time-scales, a short-term 48-hours estimate prove to be reliable in evaluating the system noise and establish a dynamic scheduling for the observations, so that higher frequency observing runs can be prioritized as soon as the weather conditions allow.

To estimate the seasonal dependency of the atmospheric conditions for radio astronomy observation purposes at the SRT site, we evaluated the system noise temperature versus frequency with high frequency resolution (less than 5 GHz steps) at four specific days of the year, taken at three-month interval (15 Oct. 2019, 15 Jan. 2020, 15 Apr. 2020, 15 July 2020). For each frequency, the T_{sys} was evaluated using the realistic frequency-dependent forward efficiency values obtained by the numerical fit to the simulated data presented in Fig. 7. The derived system noise results, obtained for these four specific days, are presented in Fig. 11. The system noise was lowest in winter (15 Jan. 2020) and highest in autumn (15 Oct. 2019). All curves show similar features, with a system noise having a large almost-flat minimum near the center of the 3 mm atmospheric window ($\approx 85\text{-}100$ GHz), and an increase towards the band edges at 70 and 116 GHz. On 15 Jan. 2020, the minimum system noise was found to be of order 100 K or lower in the frequency range $\approx 85\text{-}105$ GHz. The highest noise temperature was obtained at the highest frequency of the band, 116 GHz, and has a value >200 K on 15 July 2020 and 15 Oct. 2020.

5. Conclusions

We estimated the system noise temperature at 90 deg elevation across the 70-116 GHz band of the W-band multibeam receiver to be installed at the Gregorian focus of the Sardinia Radio Telescope, assuming a SSB receiver noise temperature $T_{\text{rec}}=60$ K, by using the program presented in [1]. The system noise was calculated at various frequencies using values of the antenna feed forward efficiency η_f :

- 1) determined by an accurate simulation conducted with the GRASP software at four frequencies. The forward efficiency depends on the blockage of the beam by the receiver cabin metallic structure surrounding the 1-m diameter radome that protects the Gregorian focus from the external atmospheric agents. A fit to the simulated η_f data points was derived and used in the calculation for the subsequent estimate of T_{sys} at all frequency;
- 2) assumed to have constant value $\eta_f=0.9$ (90% of power coupled to the cold sky);
- 3) assumed to have constant value $\eta_f=1$ (100% of power coupled to the cold sky).

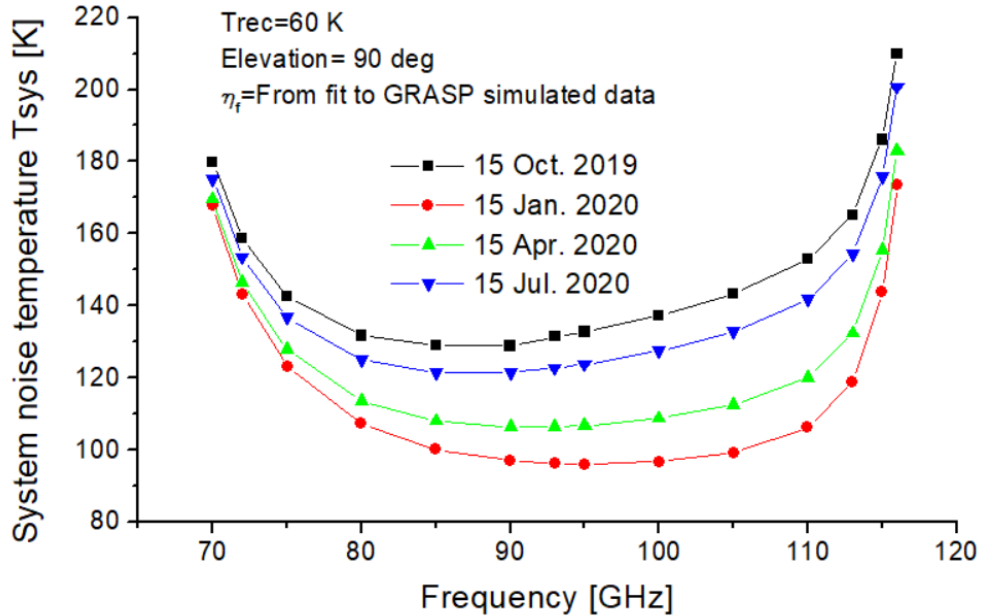


Fig. 11. System noise temperature versus frequency from the SRT site on four days of the year, three-month apart. The plots were derived assuming a receiver noise temperature of $T_{\text{rec}}=60$ K and a value of forward efficiency resulting from a fit to GRASP electromagnetic simulations of the W-band multibeam feed.

For all estimates, the truncated power that is not coupled to the sky ($1 - \eta_t$) is assumed to be terminated in an absorbing material at the physical temperature of ≈ 293 K, which adds thermal noise. It is found that the system noise temperature derived with the accurate and realistic model of η_f (calculated with GRASP) is greater than the system noise derived under the ideal and non-physical assumption of $\eta_f=1$ by only $\approx 4\%$ and $\approx 3\%$, respectively at 90 deg and 45 deg elevations at 70 GHz, where the beam truncation is greater. At 75 GHz, the corresponding fractional variation of T_{sys} are $\approx 6\%$ and $\approx 3\%$. The relative variations of T_{sys} at 90 deg elevation due to beam truncation at 93 GHz and 116 GHz are respectively, 2.6% and 0.5%. Such fractional increases of T_{sys} were obtained in the “worst case” of good weather conditions, during the winter day of 15 Jan. 2020, when the sky noise is lowest. Considering that an increase of T_{sys} by $\approx 3\%$ increases the observing time (to achieve the same source signal-to-noise ratio) by $\approx 6\%$ the effect of beam truncation and scattering by the radome is considered negligible.

Further to the added noise, the beam truncation leads to diffraction in the antenna beam pattern and might determine a standing-wave on the signal band whose effects can be reduced by covering the inner parts of the cabin around the radome aperture with radiation-absorbent material. The beam diffraction aspects are not quantitatively estimated here, and are beyond the scope of this memo.

In addition, we evaluated the seasonal variation of the system noise by calculating T_{sys} at four specific days of the year, with three-month interval, each considered to be representative of the conditions that could be met on the season. On 15 Jan. 2020, the system noise was predicted to be of order 100 K or lower in the frequency range ≈ 85 -105 GHz. In the middle of the 3 mm atmospheric window, around 90 GHz, the predicted system noise is below 140 K for all of the four selected days of the year. According to these results, it seems possible to run efficient and sensitive radio astronomy observations with the SRT in W-band over most of the year, not only during the winter season. Clearly, such W-band observations are possible only after an appropriate metrology system is in place that allows achieving high antenna efficiency and accurate pointing.

Appendix C and D presents, respectively the atmospheric opacity and the system noise estimates on July 15 2020 calculated with the program described in [1].

REFERENCES

- [1] F. Buffa, G. Serra, P. Bolli, A. Fara, G.L. Deiana, F. Nasir, C. Castiglia, A.M.S. Delitala “K-band System Temperature Forecast for the Sardinia Radio Telescope,” INAF Report N. 54, Released: 07/04/2016. Available at: <http://eonstore.oa-cagliari.inaf.it/fbuffa/report/>
- [2] I. Prandoni et al. “The Sardinia Radio Telescope: From a Technological Project to a Radio Observatory,” *Astronomy & Astrophysics*, 2017, A&A, 608, A40.
- [3] A. Navarrini et al. “The Sardinia Radio Telescope Front-Ends,” *Proceedings of 27th Int. Symp. On Space THz Tech. ISSTT2016*, Nanjing, China, 13-15 Apr. 2016.
- [4] G. Valente, T. Pisanu, P. Bolli, S. Mariotti, P. Marongiu, A. Navarrini, R. Nesti, A. Orfei, “The dual-band LP feed system for the Sardinia Radio Telescope prime focus”, in *Proc. SPIE Millimeter, Submillimeter, and Far-Infrared Detectors and Instrumentation for Astronomy V*, Vol. 7741, 774126, 2010.
- [5] A. Orfei, A. Cattani, M. Poloni, J. Roda, S. Mariotti, A. Maccaferri, A. Orlati, A. Scalambra, “Caratterizzazione del ricevitore nella banda 5.7-7.7 GHz”, SRT Memo Series GAI04-FR-5.0 May 5th, 2011.
- [6] A. Orfei, L. Carbonaro, A. Cattani, A. Cremonini, L. Cresci, F. Fiocchi, A. Maccaferri, G. Maccaferri, S. Mariotti, J. Monari, M. Morsiani, V. Natale, R. Nesti, D. Panella, M. Poloni, J. Roda, A. Scalambra, G. Tofani, “A Multi-Feed Receiver in the 18 to 26.5 GHz Band for Radio Astronomy”, *IEEE Antennas Propag. Mag.* 52(4), 62, 2010.
- [7] A. Navarrini et al. “Front-Ends and Phased Array Feeds for the Sardinia Radio Telescope,” *Proceedings of 32nd URSI GASS*, Montreal, 19-26 Aug. 2017.

- [8] A. Navarrini, L. Olmi, R. Nesti, P. Marongiu, P. Ortu, L. Cresci, A. Orlati, A. Scalambra, and A. Orfei “Design concept of W-band multibeam receiver for SRT,” *Proceedings of 31st Int. Symp. On Space THz Tech. ISSTT2020*, Tempe, AZ, USA, 8-11 Mar. 2020.
- [9] G. Cortes Medellin, “Antenna Noise Temperature Calculation,” *US-SKA Technical Memo Series, Memo 95*.
- [10] T. L. Wilson, et al., “Tools of Radio Astronomy”, 5th edn., *Astronomy and Astrophysics Library*. Springer, Berlin, 2009.
- [11] M. L. Kutner and B.L. Ulich, “Recommendations for calibration of millimeter-wavelength spectral line data,” *The Astrophysical Journal*, 250: 341-348, Nov 1st, 1981.
- [12] J. W. Lamb, “Optical study for ALMA receivers,” NRAO, *ALMA Memo Series*, No. 359, Mar. 2001.
- [13] T. Pisanu, S. Casu, P. Marongiu, A. Navarrini, G. Deiana, C. Migoni, “Misura di temperatura di rumore con diversi materiali, sulla copertura del Gregoriano di SRT”, *INAF Internal Report n. 16*, 2020-04-07T08:48:22Z, March 2020, Available at: <https://openaccess.inaf.it/handle/20.500.12386/23887>.
- [14] UKRI-RAL Space “CARUSO Optical Subsystem - Beam truncation update”, Issue 1.0, August 2020.
- [15] F. T. Nasir, C. Castiglia, F. Buffa, G. L. Deiana, A. Delitala, A. Tarchi, “Weather forecasting and dynamic scheduling for a modern cm/mm wave radiotelescope,” *Experimental Astronomy*, Volume 36, Issue 1-2, pp. 407-424, Aug. 2013.

Appendix A

The SRT optical configuration with ray tracing and the telescope layout with dimensions are provided, respectively in Figs. A1 and A2. The optical parameters are listed in Table A1.

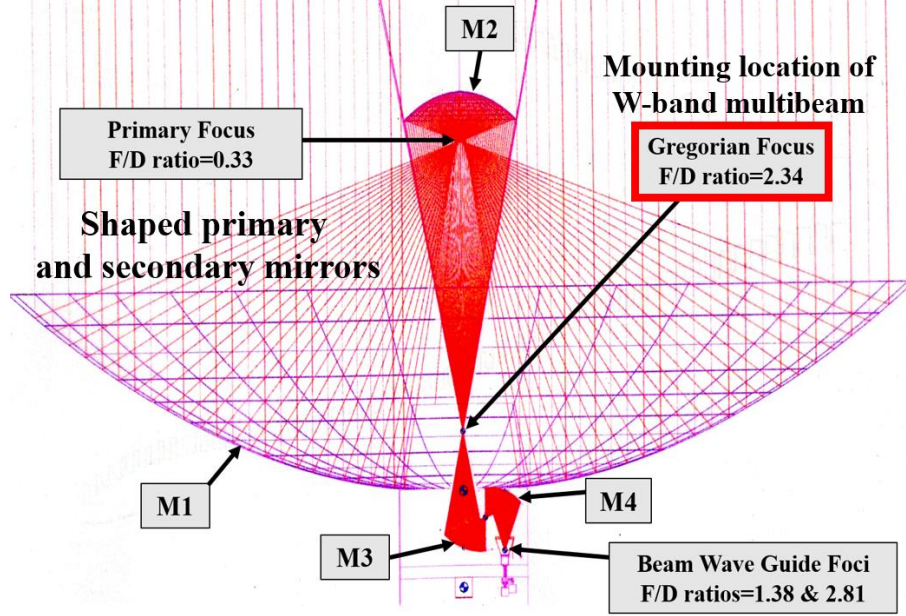


Fig. A1. Optical configuration and ray tracing of the Sardinia Radio Telescope showing the 64-m diameter primary (M1), the 7.9-m secondary (M2), and two additional Beam Waveguide (BWG) mirrors (M3 and M4). Three out of six possible focal positions (primary, Gregorian and BWG) are shown together with corresponding focal ratios. The mounting location of the W-band receiver is at the Gregorian focus ($f/D=2.34$).

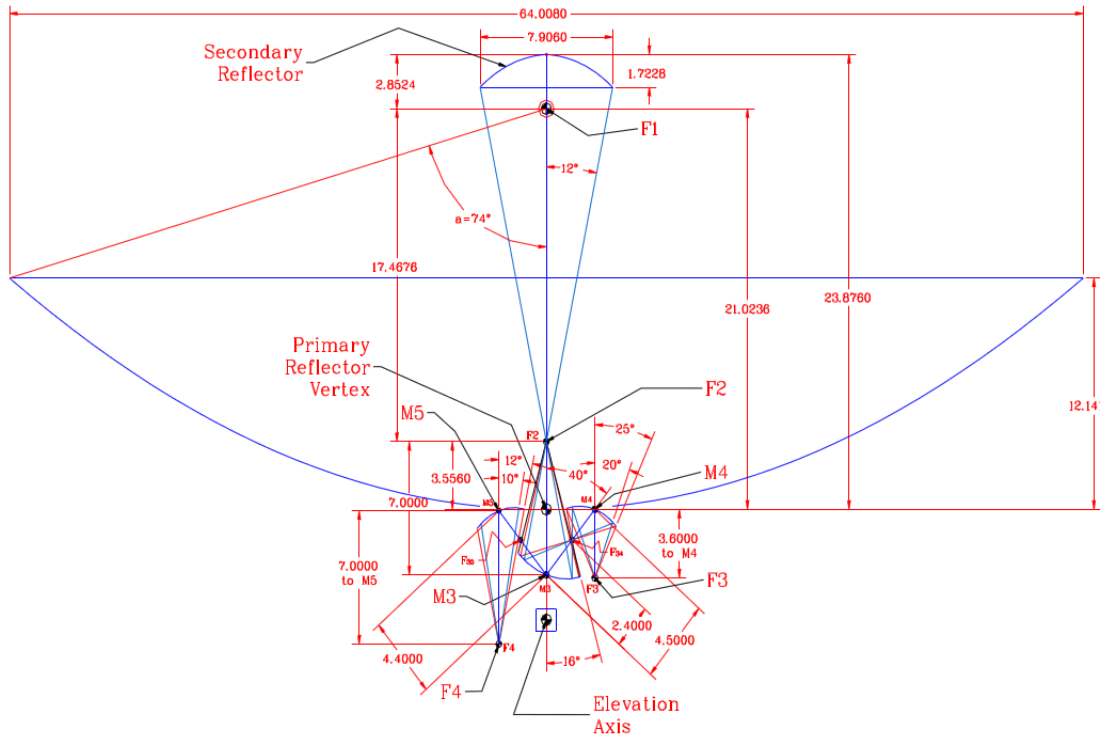


Fig. A2. Optical layout details with dimensions.

<i>Optical configuration</i>	Shaped Gregorian
<i>Sub reflector geometry</i>	Numerical
<i>Prime mirror diameter, D [m]</i>	64.008
<i>Sub reflector diameter, d [m]</i>	7.9060
<i>Focal length, f [m]</i>	21.0236
<i>Prime focus focal ratio, f_1/D</i>	0.3285
<i>Secondary focus focal ratio, f_2/D</i>	2.342
<i>Distance from Prime to Gregorian foci [m]</i>	17.4676
<i>Magnification, M [m]</i>	7.13
<i>Prime focus to sub reflector vertex [m]</i>	2.8524
<i>Secondary focus to sub reflector vertex [m]</i>	20.3200
<i>Secondary focus to primary mirror vertex [m]</i>	3.5560
<i>Distance from Prime mirror vertex to aperture plane [m]</i>	12.1415
<i>Distance from Prime focus to aperture plane [m]</i>	8.8821
<i>Prime mirror half-angle [degree]</i>	74
<i>Sub-reflector half-angle [degree]</i>	12

Table A1. Optical parameters of the Sardinia Radio Telescope.

Appendix B

Fig. B1-B2, B3 provide the system noise estimates calculated respectively at 75, 93 and 116 GHz elevations for 45 and 90 deg elevations.

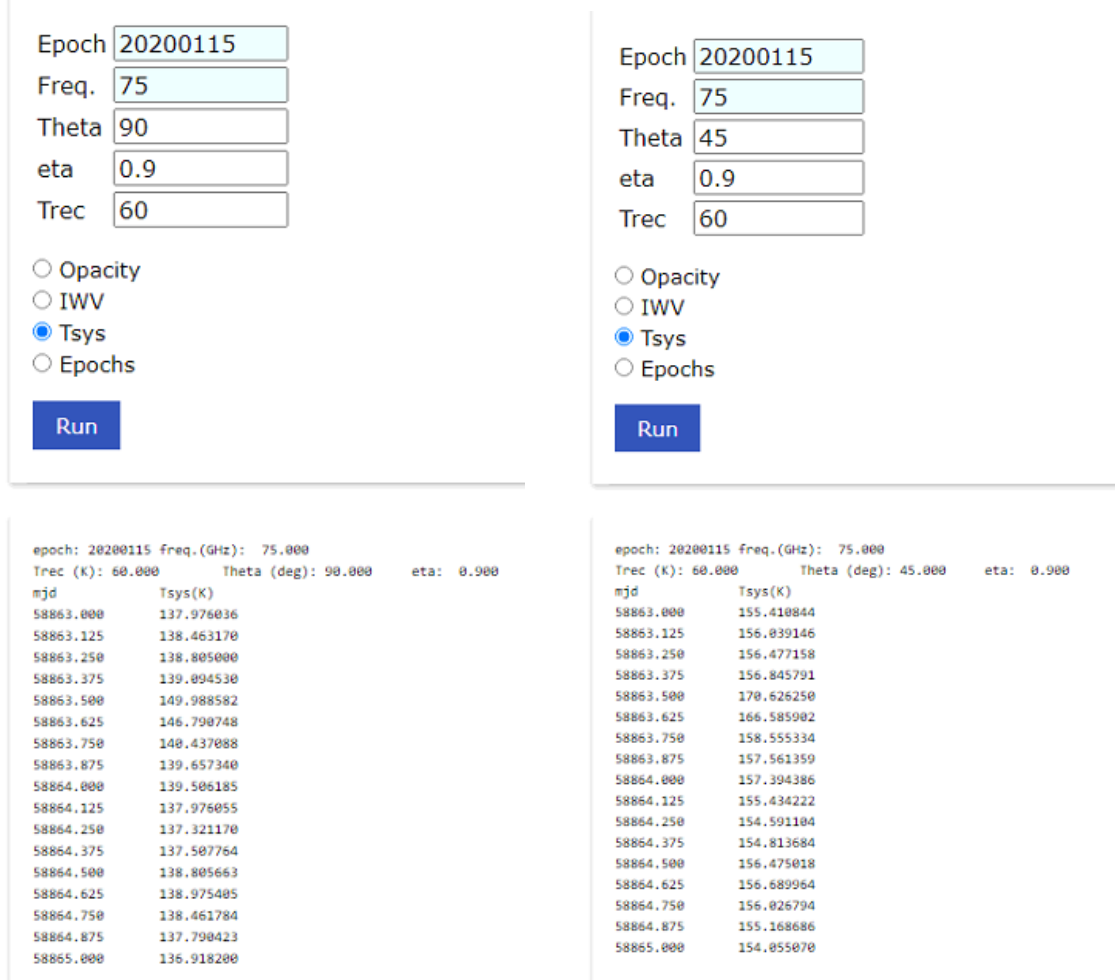


Fig. B1. System noise estimates at 75 GHz at 90 deg (left) and 45 deg elevations (right). Atmospheric data of January 15, 2020.

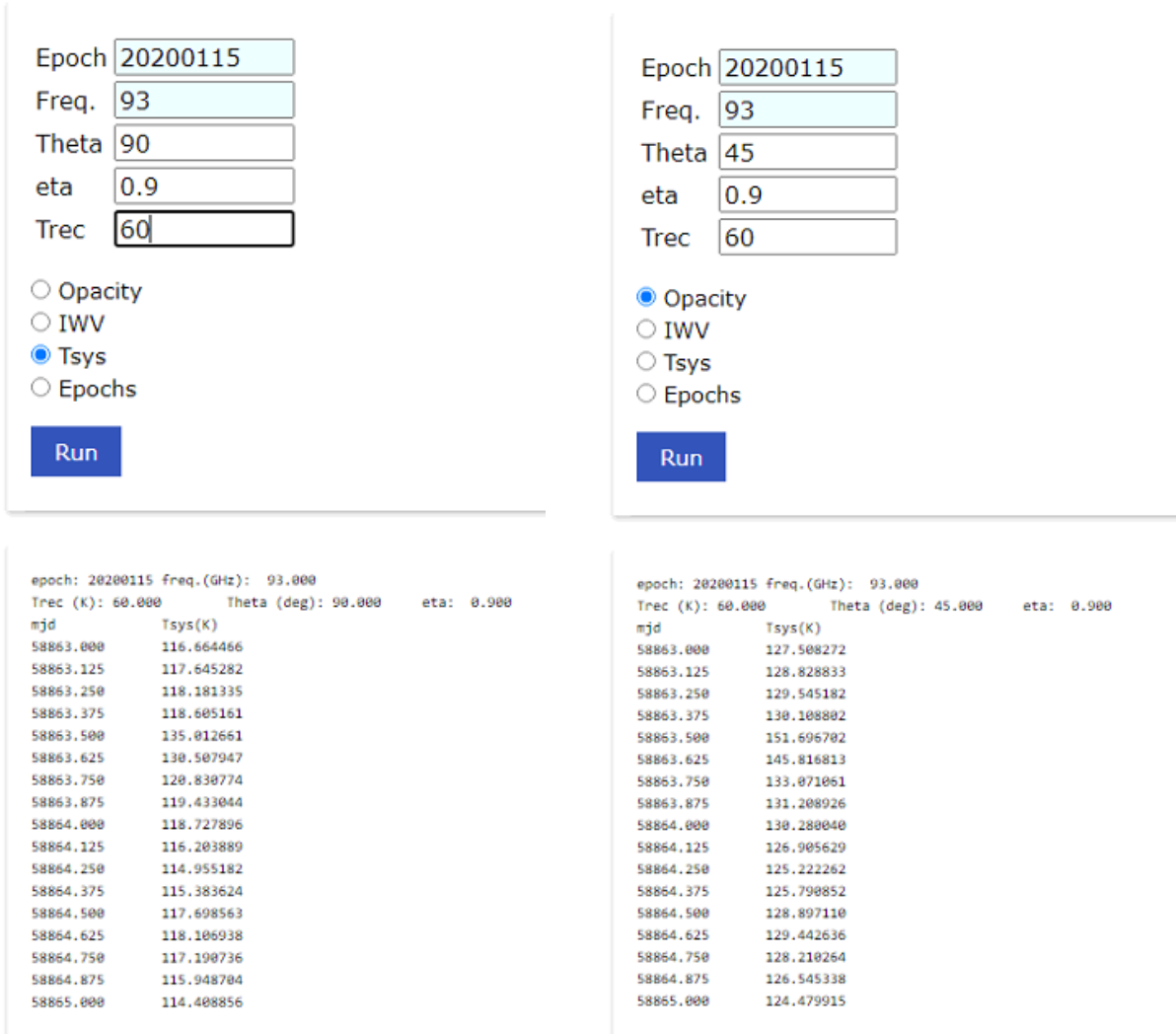


Fig. B2. System noise estimates at 93 GHz at 90 deg (left) and 45 deg elevations (right). Atmospheric data of January 15, 2020.

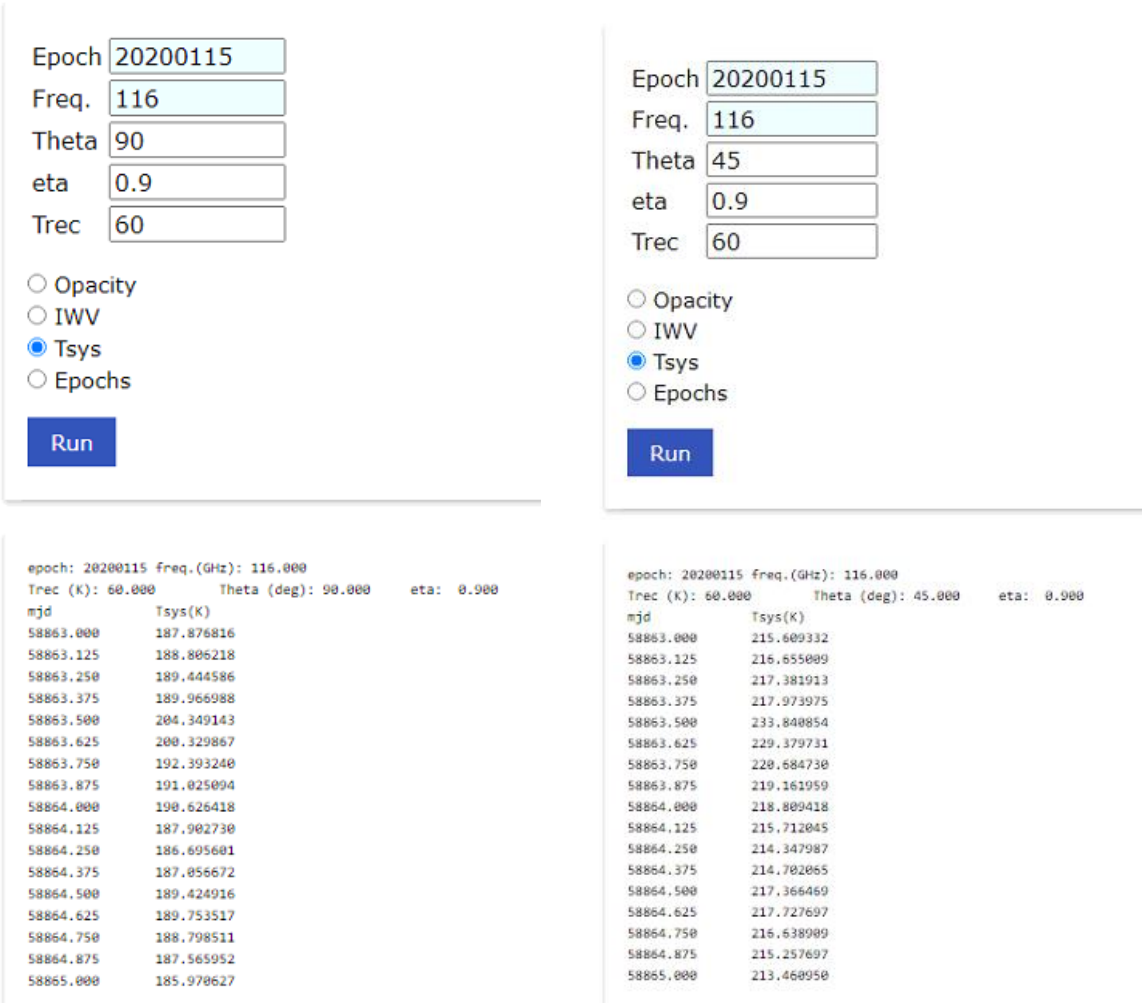


Fig. B3. System noise estimates at 116 GHz at 90 deg (left) and 45 deg elevations (right). Atmospheric data of January 15, 2020.

Appendix C

Estimates of opacity at the SRT site at 70 GHz, 75 GHz, 93 GHz and 116 GHz based on recorded atmospheric data of Jan 15, 2020, calculated with the program developed by F. Buffa. The results at the four frequencies are shown in Fig. C1.

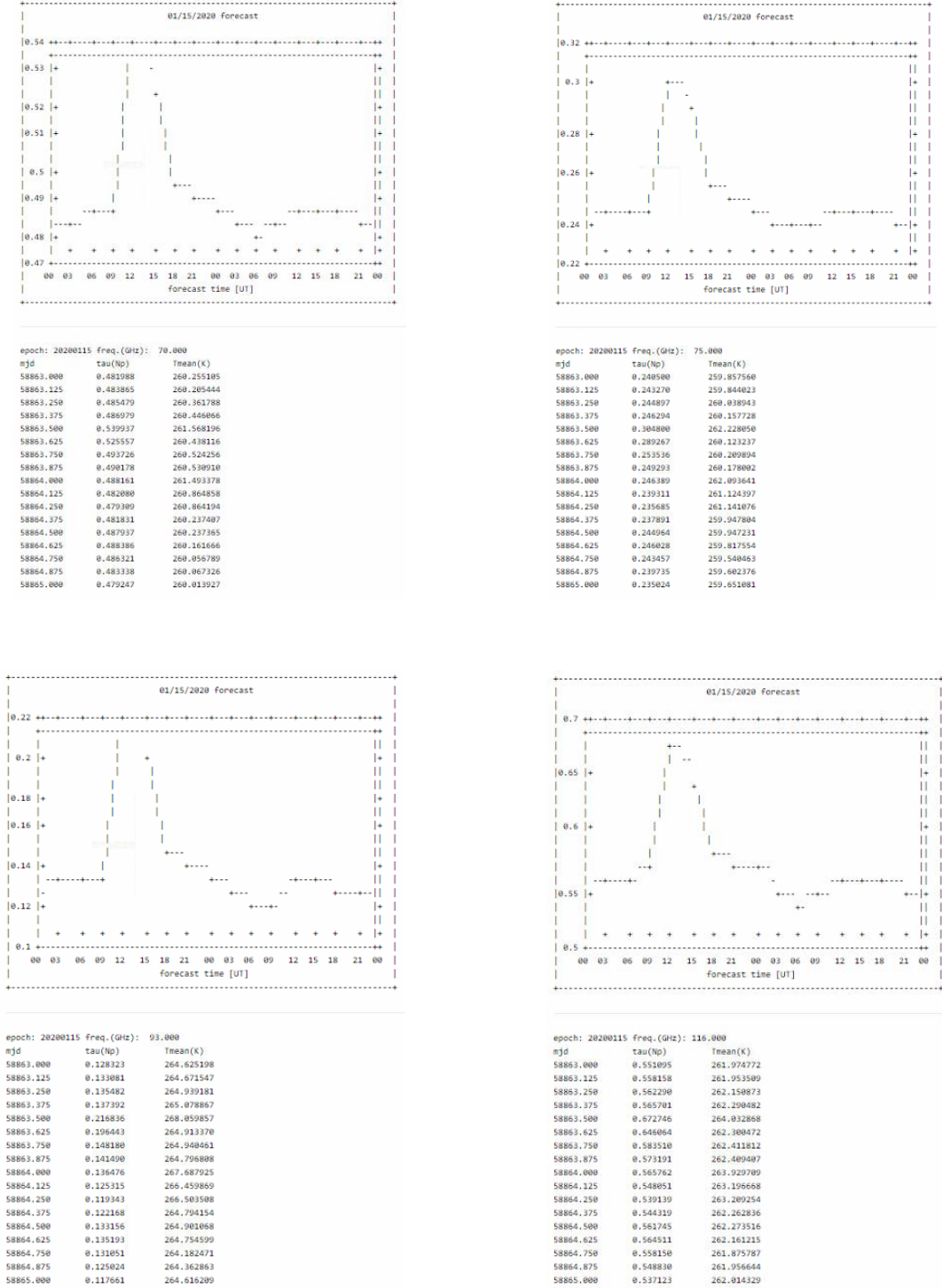
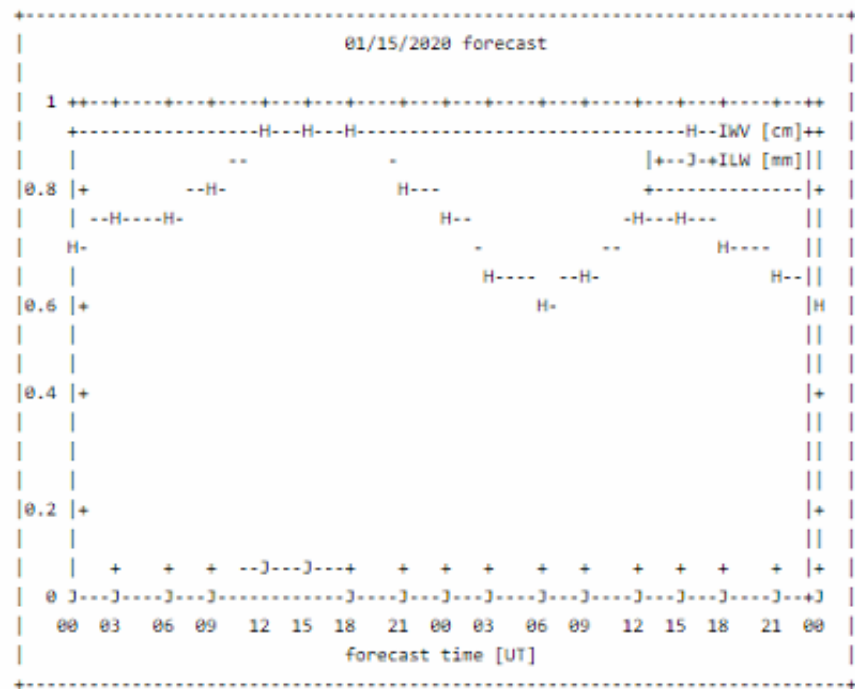


Fig. C1. Opacity at zenith versus time (expressed in Julian day) at the SRT site on January 15 2020 at four different frequencies: 70 GHz (top left), 75 GHz (top right), 93 GHz (bottom left), 116 GHz (bottom right). Values are provided in plot and table format at each sampled time.

Fig. C2 shows the variation over time of the Integrated Water Vapour (IWV) and of the Integrated Liquid Water (ILW) at the SRT site based on recorded atmospheric data of Jan 15, 2020.



mjd	IwV(mm)	ILW(mm)
58863.000	6.972870	0.000000
58863.125	7.423205	0.000000
58863.250	7.820390	0.000000
58863.375	8.163260	0.000000
58863.500	9.409614	0.065400
58863.625	9.386318	0.046622
58863.750	9.333852	0.000000
58863.875	8.488055	0.000000
58864.000	7.834983	0.000000
58864.125	6.666571	0.000000
58864.250	6.034067	0.000000
58864.375	6.301149	0.000000
58864.500	7.366585	0.000000
58864.625	7.594140	0.000000
58864.750	7.193910	0.000000
58864.875	6.614949	0.000000
58865.000	5.897473	0.000000

Fig. C2. IWV and ILW versus time. The quantities are calculated along a vertical profile and expressed in mm of condensate water.

Appendix D

System noise estimates assuming $\eta_r=0.9$, July 15th 2020

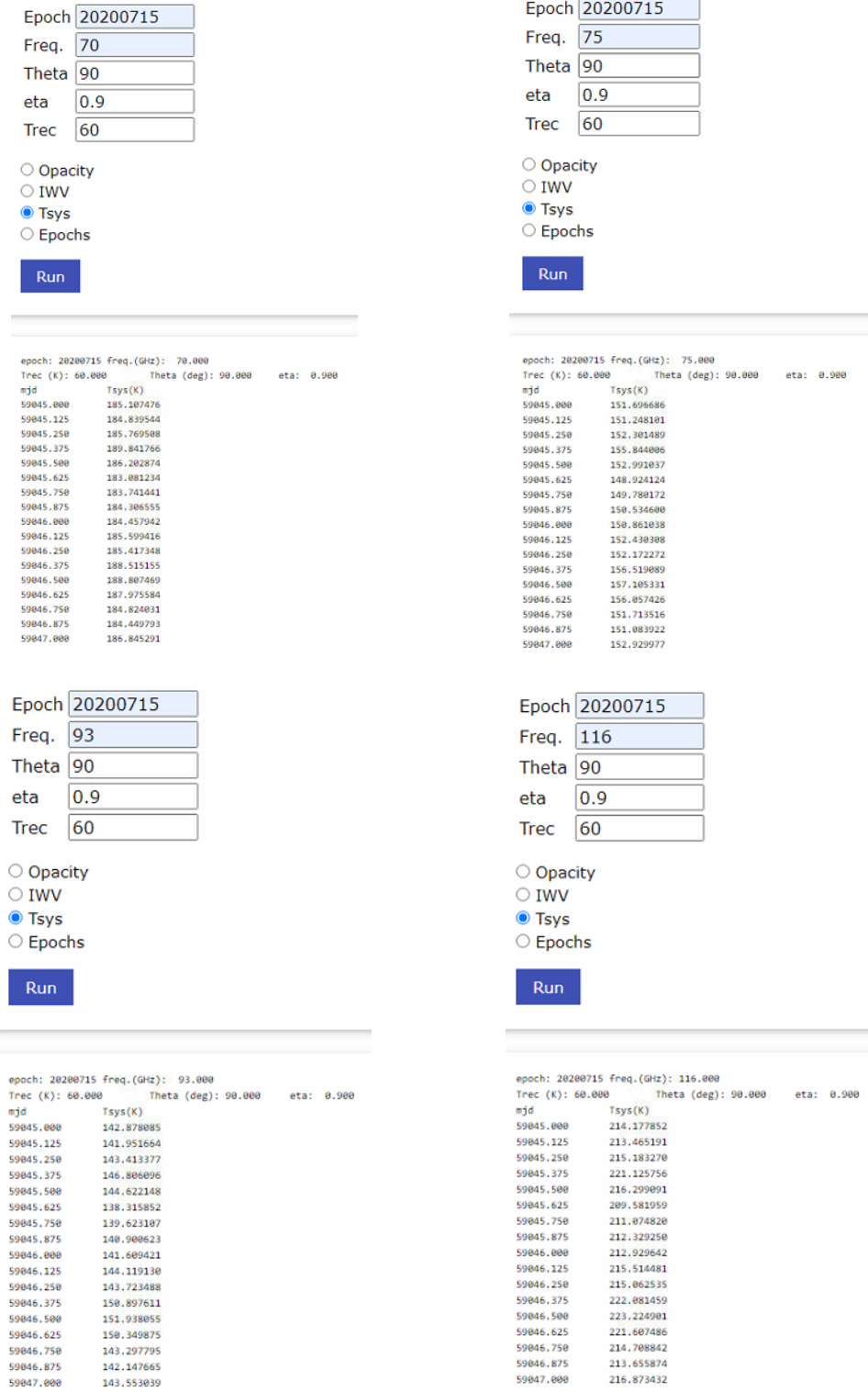


Fig. D1. System noise estimates at 93 GHz (left) and 116 GHz (right) at 90 deg elevation. Atmospheric data of July 15, 2020.

Appendix E

Following Wilson [10], the observed antenna temperature when the antenna is pointed at the blank sky (ignoring atmospheric absorption) can be written as:

$$T_A = \frac{\eta_r \iint_{4\pi} T_B(\Omega) P_n(\Omega) d\Omega}{\iint_{4\pi} P_n(\Omega) d\Omega} \quad (\text{E1})$$

where $P_n(\Omega)$ is an arbitrarily normalized antenna power pattern (for example $P_n(0)=1$) and η_r is the radiation efficiency of the telescope accounting for ohmic losses (see KU).

Following KU we now divide the antenna pattern into two zones, one involving the “normal” diffraction pattern (corresponding to a narrow region of the sky around the optical axis) and the other involving spillover (both forward and rearward) as well as scattering, so that the numerator in (E1) can be written as:

$$\iint_{4\pi} T_B(\Omega) P_n(\Omega) d\Omega = \iint_{\Omega_d} T_B(\Omega) P_n(\Omega) d\Omega + \iint_{4\pi - \Omega_d} T_B(\Omega) P_n(\Omega) d\Omega$$

If we now assume that within the diffraction pattern region Ω_d the brightness temperature is fairly independent on Ω , $T_B(\Omega) \approx \text{const} = T_{sky}$, and that in the complementary solid angle ($4\pi - \Omega_d$) it is again constant, assuming that all spillover and scattering is terminated to a single (ambient) temperature $T_B(\Omega) \approx \text{const} = T_{spill} = T_{amb}$ then it can be shown that (E1) becomes:

$$T_A = \eta_r [\eta_{fss} \eta_{rss} T_{sky} + (1 - \eta_{fss} \eta_{rss}) T_{spill}] \quad (\text{E2})$$

where, following KU, the two efficiency terms are defined as:

$$\eta_{fss} = \frac{\iint_{\Omega_d} P_n(\Omega) d\Omega}{\iint_{\Omega_0} P_n(\Omega) d\Omega} \quad \eta_{rss} = \frac{\iint_{\Omega_0} P_n(\Omega) d\Omega}{\iint_{4\pi} P_n(\Omega) d\Omega} \quad (\text{E3})$$

The double integral over Ω_0 extend to an arbitrary region, useful in practice to simplify the calculation of the T_A ; in KU original work $\Omega_0=2\pi$ is indicated as an example, so that the double integral over Ω_0 extends to the forward hemisphere (the sky), where, in most practical cases, the brightness temperature can be assumed constant (T_{sky}). The efficiency η_{fss} takes into account the part of the radiated beam in the Ω_0 region associated to the diffraction term of the antenna beam (in practice a very narrow region close to the antenna main beam). The efficiency η_{rss} , known as *forward efficiency* (and frequently referred to as η_f or F_{eff} in the literature), takes into account the part of the antenna beam radiated in the Ω_0 region, i.e. in the forward hemisphere when $\Omega_0=2\pi$.

According to the definitions in KU, a cumulative efficiency $\eta_l \equiv \eta_r \eta_{rss}$ is defined. Here, we assume $\eta_r=1$, thus $\eta_l = \eta_{rss}$.

A semi-quantitative model, more appropriate to describe the spillover in the SRT, requires to divide the antenna pattern in *three* zones, Ω_{sub} , Ω_{hole} and Ω_{cab} , as defined in Fig. 3 and Fig. 6. Thus, we can associate to each region its own efficiency

$$\eta_{sub} = \frac{\iint_{\Omega_{sub}} P_n(\Omega) d\Omega}{\iint_{4\pi} P_n(\Omega) d\Omega} \quad \eta_{hole} = \frac{\iint_{\Omega_{hole}} P_n(\Omega) d\Omega}{\iint_{4\pi} P_n(\Omega) d\Omega} \quad \eta_{cab} = \frac{\iint_{\Omega_{cab}} P_n(\Omega) d\Omega}{\iint_{4\pi} P_n(\Omega) d\Omega} \quad (E4)$$

where we have $\Omega_{sub} + \Omega_{hole} + \Omega_{cab} = 4\pi$ and, consequently, $\eta_{sub} + \eta_{hole} + \eta_{cab} = 1$

If in (E3) we assume $\Omega_d = \Omega_0 = \Omega_{sub} + \Omega_{hole}$, the diffraction region Ω_d is extended to the whole antenna beam coupled to the sky (Ω_{sub} and Ω_{hole} are terminated to the sky, thus into a region whose temperature is approximately constant, T_{sky}) and the forward efficiency is associated to the same angular region (where the antenna beam couples to the sky, $\Omega_{sub} + \Omega_{hole}$). In this case (E3) becomes:

$$\eta_{fss} = \frac{\iint_{\Omega_{sub} + \Omega_{hole}} P_n(\Omega) d\Omega}{\iint_{\Omega_{sub} + \Omega_{hole}} P_n(\Omega) d\Omega} = 1$$

$$\eta_{rss} = \frac{\iint_{\Omega_{sub} + \Omega_{hole}} P_n(\Omega) d\Omega}{\iint_{4\pi} P_n(\Omega) d\Omega} = \frac{\iint_{4\pi - \Omega_{cab}} P_n(\Omega) d\Omega}{\iint_{4\pi} P_n(\Omega) d\Omega} = 1 - \eta_{cab} \quad (E5)$$

and (E2) can be recasted as ($\eta_r = 1$):

$$T_A = (1 - \eta_{cab})T_{sky} + \eta_{cab}T_{spill} = (1 - \eta_{cab})T_{sky} + \eta_{cab}T_{cab} \quad (E6)$$

where we assumed that the cabin contribution is associated to a constant temperature $T_{cab} = T_{spill}$.

Equation (E6) differs from both (E2) and (1) in the main text, showing that the “efficiency” coefficient to be used in the estimate of T_A depends on the effective assumptions made regarding the distribution of the spillover by the feed. The η_{cab} efficiency is associated to the separation between the region where the feed radiation is coupled to the cabin and the region where it is coupled to the sky. By defining the feed efficiency η_{feed} as the ratio of the feed radiation coupled to the sky (also by means of the optics) over all the feed radiation, we obtain $\eta_{feed} = 1 - \eta_{cab}$ and we can write (E6) as:

$$T_A = \eta_{feed}T_{sky} + (1 - \eta_{feed})T_{spill} \quad (E7)$$

that is in the form used in (2) for the T_{sys} calculation.

The η_{feed} efficiency is very useful in our case because it is equivalent to the RTP parameter defined in the main text, describing the spillover by the feed inside the receiver cabin and it can be directly measured with a skydip procedure.